

Towards realistic modeling of plasmonic nanostructures: the comparative study to determine the impact of optical effects on solar cell improvement

Gholamhosain Haidari (✉ moh1135@gmail.com)

Shahrekord University <https://orcid.org/0000-0003-2400-9280>

Research Article

Keywords: Plasmonic nanostructure, Realistic modeling, Parasitic absorption loss, Near-far field effect, Organic solar cell

Posted Date: May 13th, 2021

DOI: <https://doi.org/10.21203/rs.3.rs-476910/v1>

License:  This work is licensed under a Creative Commons Attribution 4.0 International License.

[Read Full License](#)

Version of Record: A version of this preprint was published at Journal of Computational Electronics on January 20th, 2022. See the published version at <https://doi.org/10.1007/s10825-021-01829-x>.

Abstract

Plasmonic structures may improve cell performance in a variety of ways. More accurate determining the optical influence, unlike ideal simulations, requires modeling closer to experimental cases. In this modeling, nonregular nanostructures were chosen and for simulation divided into three groups and some modes. For each mode, different sizes of nanoparticles were randomly selected which could result in pre-determined average particle size and standard deviation. By 3D-FDTD, the optical plasmonic properties of that mode in solar cell structure were investigated when nanostructure was added to the buffer/active layer of the organic solar cell. The far and near-field results were used to compare the plasmonic behavior, relying on the material and geometry. By detailed simulations, the Al and approximately Ag nanostructure at the interface of the ZnO/active layer can improve OSC performance optically, especially by the near-field effect. Unlike Au and relatively Ag, the Al nanostructured sample showed less parasitic absorption loss.

1. Introduction

Crises may always arise in human society and pose serious emergencies to us, for example, one of them is the spread of the Quid-19 virus in 2020. Such cases remind us that restrictions must always be considered before they become serious crises. Today, researchers warn of current limitations on energy, environmental, and related economic issues that could lead to serious crises in the future [1]. Interestingly, solar energy has sufficient potential to prevent such crises [1, 2]. Research on photovoltaics has led to the offering of several different types of solar cells [3]. In photovoltaic research, increasing efficiency-longevity and reducing costs have always been considered in research works. The organic solar cell (OSC) has emerged as one of the leading kinds in this photovoltaic internal competition [4]. Meanwhile, silicon-based cells are involved in the cost of materials and their processing. Also, perovskite cell has had great growth in efficiency, but they have not shown good stability so far. Therefore, the organic cell has still considered a viable alternative for first-generation cells [5, 6]. It is possible to produce roll-to-roll and economy, lightweight, with flexibility and proper efficiency-stability with organic cells [3, 4]. However, OSC efficiency is relatively low compared to other competitors. Low carrier mobility in most organic semiconductors limits the thickness of the active layer, which in turn decreases light absorption [4]. Therefore, increasing the light absorption of organic semiconductors has become a challenge due to this limitation. In 1998, Stuart and Hall observed that by introducing silver nanoparticles (Ag NPs) on the surface of the silicon photodetector, nearly a factor of 20-fold enhancement in photocurrent was obtained. The results meant that metallic NP(s) could induce local surface plasmon resonance among themselves and scatter light [7]. This outcome is very significant in light-harvesting applications such as water splitting, thermoelectric, photovoltaic, photocatalytic, and photodynamic therapy [8]. In the field of photovoltaics, such as OCS, the metal nanostructures (MNSs) may act as a light-trapping mechanism [9–11]. They can enhance the absorption in the active layer while the thickness is still very thin (around 100 nm). MNS(s) with various sizes and morphologies have been generally used in photovoltaics to activate plasmonic consequences [12]. Depending on their position inside OPV, it usually leads to three distinct

optical mechanisms, namely (i) light scattering, (ii) localized surface plasmon resonance (LSPR), (iii) surface plasmon polariton(s) SPP(s). However, metal nanoparticles (MNPs) can be the origin of non-optical effects inside the cell. They can have other positive or negative effects on solar cell (SC) performance. On the other hand, the plasmonic structures are sometimes associated with other effects, such as electrical effects (like plasmon-induced charge separation, change surface resistance, change in electron-hole transition, change surface recombination, and changing morphological ones) [9, 11, 12]. Therefore, by mixing various effects, improving the performance of the OSCs through metallic NS(s) can be a complex mechanism. For the OSC, the MNSs have been inserted into relatively distinct positions: into the buffer or active layer, at the bottom interface between the active layer and the metal electrode, or the interface of two layers. If the plasmonic enhancement more focuses on further scattering of the incident light into the active layer, the MNSs can be placed on (i) the interface of the transparent conductive layer (TCO) and carrier transport layer (CTL), (ii) directly inside CTL or (iii) interface of CTL-organic active layer. Concerning the material selected for this purpose, most Ag and Au NSs have been used to date. Both metals have good chemical stability and have been studied in various ways to make regular and irregular NSs [13]. But for these noble metals, plasmonic wavelength (and most likely parasitic absorption) is usually in the visible region, where it often overlaps with the absorption region of the active layer. In practice, the plasmonic resonance modes of a nanoparticle can result in either forward-backward scattering or parasitic absorption. The latter does not contribute to solar cell enhancement, but rather leads to an optical loss. For the light trapping effect, plasmonic NSs should play a scatter role. Aluminum (Al) has emerged as an alternative metal due to its low cost and LSPR in the UV spectral region. For example, according to Mie's theory, for a sphere with a diameter of 60 nm of Ag, Au, and Al in the air, extinction peaks occur at 380 nm, 504 nm, and 208 nm, respectively. Al is a non-resonant plasmonic metal, which means that the LSPR of Al may be more easily engineered. So, it cannot interact with the larger amount of incident light (i.e., visible spectrum), and consequently, plasmon-induced losses by parasitic absorption would not occur. Al is recognized to be very acceptable scatter for use in photovoltaics. In 2010, the effects of resonant (Ag) and non-resonant (Al) plasmonic NPs in a thin-film hydrogenated amorphous silicon (a-Si: H) solar cell were studied [14]. In 2014 the enhancing of the optical absorption of the dye-sensitized solar cell (DSC) by Al NS was investigated [15]. For preparing MNSs, depending on the desired size and geometry, many physical and chemical fabrication methods have been used [16]. Each of these methods has its advantages and disadvantages. For example, the thermal evaporation method is a simple-clean and environmentally friendly method for preparing NSs [16]. The potential plasmonic advantages of Al NS over Ag and Au, depend on its plasmonic wavelengths. But, that is a function of the size, shape, and surrounding material [12]. Therefore, determining the plasmonic wavelengths and applicability of prepared metal NS in an SC will be of great importance. In this study, using the 3D-FDTD simulation method, the plasmonic effect of Al for improving the performance of organic cells was investigated. These MNSs can be located in the TCO/CTL and CTL/active layer interface with different methods. In this study, MNS modeling was performed so that it could properly represent somewhat regular NSs can formed by some methods. Therefore, this modeled MNS tried to be very close to experimental ones. To better clarify the plasmonic effect, the near and far-field simulated effects of Ag and Au NSs (with a similar structure) were compared with Al's counterparts.

Moreover, the outcoming of this research could help to guess the optical effect of Al, Ag and Au NSs in a variety of solar cells, such as Dye-sanitized and perovskite solar cells.

2. Theory And Modeling

2.1 Aluminum against noble metals

Noble MNSs such as Au and Ag have been widely used in plasmonics due to their relative ease of production. In contrast noble metals, Al is low-cost and generally available as it is very abundant material on Earth. Noble metals may show a negative optical effect and reduced performance of the SC in the LSPR wavelengths. It is due to the absorption losses. However, may show a positive effect and photocurrent enhancement in the off-resonance section of the NPs. The resonant wavelength of Al is located at UV but can be extended to visible or even NIR [17]. Moreover, Using Al plasmonics has properly been increased in recent years [18]. Colloidal chemistry of Ag and Au, based on salt reduction, is broadly employed in various applications in nano-optics. In contrast, the chemical synthesis of Al-NP seems not a common method since the reduction of Al salts is complicated [19]. Simple metal evaporation followed by different thermal annealing and masking techniques can lead to the formation of well-separated NSs over large areas [20–22]. Although the annealing and via a mask can lead to a relatively regular pattern of NSs, in general, this method points to NSs with nearly diverse distribution in shape and size.

2.2 The glance of conventional modeling

In numerical Electromagnetics, a method such as finite-difference time-domain (FDTD) is beneficial when a broadband analysis is required like the SC. The FDTD method uses the central difference approximation to discretize the Maxwell equations, in both the time and spatial regions and then derives the electric and magnetic field distributions in the Yee cells at each time step [23, 24]. In a conventional FDTD SC simulation, the 3D simulation cell includes different thin-film layers of the cell (for example, along with the x-z direction), and the plane wave source is usually polarized along with thin films and propagates in the y-direction. Therefore, the x-z periodic boundary conditions (PBC) are selected in line with the thin layers, and the perfectly matched layer (PML) boundary condition is selected perpendicular to them (or in the y-direction). The PML is one of the advantages of the FDTD method compared to the finite element method (FEM), making it possible to more appropriately simulate problems that have unclosed-space [24]. Different dispersive materials are identified in the simulation cell due to their complex refractive indexes. Moreover, it is possible to calculate the reflection-transition spectra and parasitic absorption of different layers by the simulation data. This type of calculation can be done to some extent with a simpler method such as the transfer matrix method (TMM). FDTD capabilities manifest when the optical model tries to contain more detail, as it moves away from those as mentioned earlier (1D photonic crystal). Simulation of plasmonic SC is one of the cases where the FDTD method has proven its ability to simulate the near and far-field as well as surface plasmon polariton (SPP) effects [23]. Plasmonic SC mainly refers to the use of plasmonic NSs to overcome the limitations of third-generation SCs. The organic solar cell (OSC) is a valuable kind among the third-generation cells, that its

efficiency needs to increase more. Balancing between the exciton diffusion length and the absorption of the active layer of the OSC leads to the detail that thicknesses of more than 100 nm for the active layer should not be selected. So, this leads to low absorption of the active layer. Hence, it is necessary to think about increasing the absorption without physically increasing the thickness of the active layer [12, 25]. Initially, more attention was paid to the light trapping due to the plasmonic NSs. Still, they can be involved in improving the performance of organic SC through various optical, electrical, and structural mechanisms [10]. However, optical effects can be considered one of the most important ones. There have been some simulations about the optical study of MNSs concerning SCs. These MNSs can be added at different SC locations, and depending on the location, the near and far-field effect or both on the efficiency of the SC can be examined [9–11]. In the far-field approach, the reduction in backward scattering is generally simulated, leading to an increase in the optical absorption of the active layer. Whereas in the near-field approach, the determination of wavelength(s) of LSPR is the simulation's goal. In normally simulated structures, they mainly consist of structures composed of single-particle (like a sphere or hemisphere) and sometimes periodic nanostructures (NSs) [26]. Concerning a single particle, the simulations can only be practical regarding the particle distribution with a considerable distance (single-particle approximation). However, if more attention is paid, the experimental samples don't have NPs with the same shape. It cannot be expected that the near-field distribution around all of them will be the same, limiting the applicability of the results of such simulations to some extent. Moreover, about periodic structures, the results of far-field simulations depend on the shape, size of the NS, and the periodic distribution. Again, in an experimental sample, one cannot expect a periodic structure to be exactly the same as the numerical optimized structure. On the other hand, the results of such simulations will show more weaknesses, especially, when it comes to simulating accurately experimental periodic NSs. In fact, in the often method of NS fabrication, the shape, size, and periodicity distribution of the MNS will be to some extent wide. Therefore, the right FDTD modeling of these nanostructures will have its challenges.

To answer this challenge in this study, due to the experimental data concerning experimental MNSs [14, 17, 18, 20, 21, 27, 28], firstly, elliptical nanoparticles were chosen and divided into three groups based on the oblate or prolate form. Moreover, due to vertical height, some modes were considered for each group. For each mode, different sizes of nanoparticles were somewhat randomly selected which could result in pre-determined average particle size and standard deviation. They were put on the interface of the ITO/buffer layer and buffer/active layer, respectively. This type of modeling can represent to some extent orderly MNSs that can be formed by different experimental methods.

2.3 Details of this modeling

In the fabrication of nanostructure, the nucleation mechanism of thin-film growth has been classified into three major types (Vander Merwe or island growth mechanism, Volmer Weber or layer mechanism, and Stranski-Krastanov mechanism) depending on the interaction between the deposited atoms of the target and the surface of the substrate [29]. The metal forms the NS shape since the thickness ($< \sim 30$ nm) is not thick enough to form a continuous film [20]. Atoms undergo a series of kinetic processes, start to

initiate nucleation, and island formation. The nanostructure fabrication method can be associated with various conditions, such as heating the substrate during formation, annealing. For example, thermal evaporation by using different masks leads to more structured arrangements and separate NPs. In some fabrication methods depending on the different conditions, particles can form a shape similar to an ellipsoid (or part of it) and with different contact angles. On the other hand, the review of AFM and SEM images in the literature suggest that the ellipsoidal NPs for modeling experimental NS could be a suitable choice [14, 17, 18, 20, 21, 27, 28, 30, 31]. These ellipsoidal NPs are some extent, randomly distributed in shape, size, rotation, and distance from each other. Usually, average values of these geometrical factors are used for modeling, i.e. the distribution of identical NPs with an average size at a constant distance (average distance) from each other [31]. However, since the plasmonic properties are very dependent on the shape, size, and distance distribution of the NPs, the conventional methods cannot be efficient for the simulation. Therefore, in this study, an attempt has been made for more accurate modeling of these kinds of MNSs. Consider NPs by combining ellipsoids with the random distribution (i.e., to some extent random ellipsoids in shape, size, rotation around vertical axes, and distance). Shorty in this modeling, the NPs were divided into three groups: oblate ellipsoid, prolate ellipsoid, and oblate spheroid (O, P, and S). For each group, some modes (specified with a number like 1,2,3, and 4) were considered, as shown in Fig. 1. These three groups and their modes are somewhat reminiscent of different S (different particle heights, elongation, or oblation and different contact angles) can be deposited on the substrate by the different experimental methods. Therefore, the simulation of these states will be beneficial to predict the near-far optical field effects of such structures. Mean particle sizes with their standard deviation supposed for each mode are listed in Fig. 1. Then, assuming the proper average particle sizes and their standard deviations for each mode, some nanoparticles were chosen for making MNS. Figure 2 shows the 3D perspectives and XY-XZ view of one typical MNS of one mode. This figure also shows the cross-section planes perpendicular to the XZ surface (normal cross-section).

2.4 Simulation features

Fig. 3 shows the 3D-FDTD model of OSC: ITO/ZnO/MNS/PTB7-PCBM/MoO₃/Al. The plane-wave source and the FDTD region with the perfectly matched layer (PML) in the y-direction and Bloch boundary condition (BC) in the XZ surface are shown. Bloch BC is very similar to periodic BC, but because of the random distribution of MNS, while copying the fields from one edge to the other they also apply a phase correction to the fields. In the model, the flux monitors are located on the top outside of the structure for the measurement of reflected light (backward scattering) at various wavelengths. For far-field like total reflection, the results were presented after averaging on the data of ten simulations. In these ten simulations for each mode, the random distribution of particles was different from each other, but the mean values determining the distribution characteristic of metallic NS remained identical. The FDTD approach includes responses from a wide range of frequencies that are widely used for numerical simulation of the optical properties of the plasmonic NS with a single run. The Lumerical simulator is used for FDTD simulation. To better consider the NS in simulation, the override mesh setting ($2 \times 2 \times 2 \text{ nm}^3$ Yee cell) was applied to this section of the OSC model. A cross-section surface that includes the y-z axes was also selected for typical monitoring of the near-field (Fig. 3). On the other hand, the maximum

amount of field-intensity (E_{max}^2) on this surface was recorded at each wavelength. The random distribution of particles in terms of number, size, and distance depends on the selected cross-section. Thus, the geometry of the NS and therefore the near-field on each plane can be different. In other words, the near-field intensity will vary from one surface to another surface. Hence, the calculated E_{max}^2 on this selected surface can compare the near-field effect when the material of particles changed among Ag, Au, and Al.

3. Results And Discussion

3.1 Planar standard solar cell

Since the FDTD is a space and time-domain technique, the fields are calculated as a function of time across some spatial regions within the simulation. Then, the Fourier transform gives the fields as a function of frequency (spectral calculation). By propagating power across the surface, the normalized transmission-reflection can be calculated, Fig. 4 shows the total reflection curve of the standard SC structure introduced in Fig. 3 (without the presence of the MNS). This curve, because of the coherence interference, has peaks and valleys and can be engineered according to changing the thickness of layers and dispersive reflective indexes. For standard SC with a thin-film structure, the correspondence of the FDTD with the TMM method is well seen in Fig. 4. The optical power absorbed per unit volume can also be calculated by the FDTD. The photon absorption rate is equivalent to the generation rate when it is assumed that each absorbed photon excites an electron-hole pair. In the inset of Fig. 4, the generation rate is shown along with the active layer of the standard SC, that the highest rate being around its center. In the standard cell, the ideal J_{sc} (short circuit current) of 14.67 mA/cm^2 was calculated. With the addition of MNS, the assumption of 1-D photonic crystal of the cell (or TMM method) no longer be sufficient, and therefore the FDTD technique was used for other results.

3.2 Plasmonic NS (MNS) at the interface of ITO/ZnO, far-field

In the following, the far-field results (total reflection) of plasmonic cells of the O-group (different modes, 0.1-0.4) are shown in Fig. 5, while the material of the plasmonic structure is Al, Ag, and Au, respectively. In this part, the MNS is at the interface of ITO/ZnO. As shown in Fig. 5, none of the O-group of MNS can't cause to reduce the reflection across the whole spectrum than the standard cell. Also, in modes 3 and 4 of the O-group, the difference between the reflection curve of plasmonic samples and the standard one becomes less. In 0.1 and 0.2 from the wavelength of 660 nm onwards, a decrease in the reflection curve than the standard sample is observed. The largest drop is for Au, then Ag, and finally Al. This behavior is more or less seen for 0.3 and 0.4. Only the Al sample had reflections below the standard curve in the wavelength range between $\sim 400 \text{ nm}$ and $\sim 500 \text{ nm}$. The simulated far-field results for groups P and S are also shown in Fig. S1 and S2 (supporting information).

In P-group, except for mode P.2, there is not much change in the reflection curve than the standard one. In P.2, a decrease in the reflection curve is observed only in the range of 380 nm to 530 nm, especially for Al.

The total reflection comparison of the O, P group, and the standard cell shows the shape impact of MNS shape on the far-field effect. Compared to Fig. 5 and Fig. S2, there is not much change in the far-field behavior of groups O and S. The area under the reflection curve in the range of 350 nm to 800 nm can be introduced as a quantity for relative comparison. The normalized value of this quantity to the standard cell (A_i/A_s) is given in the Supporting Information (Fig. S3). In other words, the lower of A_i/A_s means the higher of forwarding scattering due to the MNS. It is shown that for Ag, the size of this quantity is more than one in O and S-group and less than one in the P-group. The opposite behavior is right for Au. For Ag, the rate of change in this quantity from O-S to P-group is more significant. What has been shown for Al is that this quantity is less than one for all three groups and its behavior is more uniform than two others. Therefore, compared to Ag and Au, Al with less dependence on its geometry, is more significant to reduce the backward reflection.

Moreover, the lowest A_i/A_s is for mode 2. In fact, in mode 1 than the other modes, the height (in the c direction) of the NS is complete, so they refer more to nanoparticles prepared using methods such as the chemical method. From the viewpoint of contact angle, in mode 2 the contact angle is more than 90 degrees (little wetting), in mode 3 the contact angle is 90 degrees and in mode 4 the contact angle is less than 90 degrees (good wetting). Therefore, depending on the ratio of the height of the NP to its lateral surface and material, engineering the contact angle of NSs can be considered as one of the factors for the effective scattering of light into the active layer.

3.3 Plasmonic NS (MNS) at the interface of ITO/ZnO, near-field part, maximum field intensity

In the following, the near-field of the introduced MNS (group O, P, and S) was studied. For this purpose, some cross-sections were selected. These cross-sections are shown in Figs. 2 and 3. On different points of these surfaces, the intensity distribution can be calculated at each wavelength. It is also possible to compare the maximum field intensity (E_{max}^2) on these cross-sectional surfaces in terms of wavelength. Indeed, the near-field result is due to the presence of plasmonic structures and usually occurs near and between them. Due to the somewhat disperse distribution in the size and position of the nanoparticles, these cross-sections will undoubtedly show different forms of NPs from one surface to another. Therefore, the near-field results will vary for each one. However, to compare the results of the introduced models of the MNS in the solar cell, such simulated near-field results can be useful. Figure 6 shows that on the selected surface of the O-group with different materials, at what wavelength, the field intensity is maximized. This near-field effect is a result of the slice of MNS in the cross-section as well as other adjacent parts of MNS that do not exist on this surface. Al has been recognized as the deep UV plasmonic material, but it is also able to be tuned as new visible-plasmonic material. As can be seen for Al, primarily due to the plasmonic NS in an environment with a higher refractive index than air ($N_{ZnO} \sim 2.4$) in the SC structure, the peaks of maximum near-field intensity are extended to higher wavelengths than the bulk case. The presence of multiple peaks at spectral maximum intensity can depend on numerous factors in the MNS, such as NP size distribution, a different form of NP coupling, bipolar resonance, and higher modes such as quadrupole as well as longitudinal-transverse excitations [32, 33].

As the height of the nanoparticles decreases in different modes of the O-group (0.1 to 0.4), the location of the peaks shifts so that the peaks become intensive at larger wavelengths. In Ag-O.1 and Ag-O.2, peaks are seen throughout the visible spectrum. By changing the mode to Ag-O.3 and Ag-O.4, the number of peaks drops, and the peaks with high intensity will be out of the visible spectrum. The same pattern (more or less) is seen for Au. Since the bulk plasmonic wavelengths for Au, start almost in the middle of the visible region (unlike Ag, which begins at about 400 nm). Therefore, Au up to 550 nm has not a significant near-field effect in none of the modes.

For Al, there are peaks throughout the visible spectrum, and for all four modes. In terms of the numerical value of the peaks, higher intensities are for Au, Ag, and Al, respectively. The spectral maximum field intensity for group P and S are given in Fig. S4 and S5, respectively. The difference between the O and S group is mainly in their lateral elliptical and circular shape. This change in MNS geometry, although cause little differences in the far-field simulation (Fig. 5 and S2), show the near-field changes are much significant. The far-field results of the P-group do not demonstrate much difference in the total reflection spectrum with the standard one (Fig. S1). In contrast, Fig. S4 shows that this structure can be associated with significant effects in the near-field domain. One of the significant differences in NS geometry between O, S, and P-group can be considered in the ratio of diameter to height of NPs. The P-group represents more prolate particles and less surface coverage than other groups. As can be seen in Fig. S4, the lower number of peaks and to some extent lower widths, indicate that the coupling effects and generally the effect of adjacent NPs are relatively less in this case. In other words, due to the greater distance among the NPs (or lower surface coverage), this state is closer to the approximation of the independent particle. Therefore, P-group shows apparent differences between its near-field effects and other groups. In the p-group (three modes), the field-intensity scale is larger than the other two groups, especially for Au. At first sight, this may be attributed to the effects of adjacent particles on each other (selected cross-section for the P-group has more particles than O and S-group). But given that the distance between the particles is considerable, this assumption cannot be extreme (the highest intensity was also observed inside the NP). Also, among the three modes of p-group (Fig. S4), P.2 shows a much greater superiority, highlighting the importance of NP geometry.

3.4 Plasmonic NS (MNS) at the ITO interface/ZnO, near-field part, the field intensity image

In the extension of the near-field study, at the same cross-sectional surfaces where the spectral E_{\max}^2 was calculated, the electric field intensity (E^2) on these surfaces at specific wavelengths (400 nm, 500 nm, 600 nm, 700 nm, and 800 nm) are simulated and presented for some modes. Figures 7 and 8 show these intensity profiles for O.2 and P.2 mode for material Al, respectively. To compare the near-field effect, similar images for the standard cell are shown in Fig. S6. In the standard cell at a wavelength of about 400 nm, the field intensity above the active layer is also significant. As the wavelength increases, the intensity increases further in the middle of the active material. These images of the field intensity at different points on the cross-sectional surface show the effect of the near-field at that specific wavelength. The field intensity is the result of the interaction of light inside the cell structure with the

NP(s) shown on the cross-section as well as other particles present in the MNS but is not exist on the selected surface. As can be seen, the intense near-field effect is more lateral and in the vicinity of NP(s), especially when the nanoparticles are very close to each other (coupling NPs).

By moving away from the MNS to the active layer (~ 10 nm), the near-field effect decreases rapidly. But, in the opposite direction, the intensity of near-field effects reduces slower. It seems that in O-S modes, the MNS doesn't lead to greater near-field intensity in the active layer, than the standard one. Here it appears that a slight change in MNS geometry can lead to a distinct change in near-field effect. In contrast to the far-field effects, which in some modes resulted in a little difference between the total reflection of the plasmonic sample and the standard one. Comparing O.2 and P.2 images (Figs. 7 and 8), as well as compare both with the standard one (Fig. S6), can be used to view differences. For the P.2 sample, intensity attenuation toward the active layer occurs more slowly in the active region of the solar cell. This can be attributed to the different geometry of the MNS and its lower surface coverage. Moreover, similar field intensity images for O.2 and P.2 modes are given in Fig. S7-S10, for Ag and Au material. It can be seen that changing the material but in the same mode, changes the appearance of the near-field. In O.2 mode, it is observed that for Al and Ag there are near-field effects for all five selected wavelengths. But for Au, strong near-field effects are more seen at 700 nm and 800 nm. These results are somewhat in line with Fig. 6, where the maximum intensity wavelengths of Au are mostly seen at around 700 nm and 800 nm, too. The same comparison in P.2 mode for three materials shows more exciting changes. In Fig. 7, in the four selected wavelengths, the field intensity inside themselves the MNS doesn't show a significant value. But for P.2 mode, especially at image related to the wavelengths of 400 nm and 500 nm for Ag (Fig. S8) and wavelengths of 600 for Au (Fig. S10), there is a significant field intensity within the MNS. This significant field intensity inside the structure can be led to parasitic loss absorption. Therefore, this behavior of the P.2 mode (for Ag and Au compare to Al) can be considered as a negative effect on the application in the plasmonic SC design.

3.5 Plasmonic NS (MNS) at the interface of ZnO/active layer of organic solar cell

Lastly, to evaluate the differences, the MNS (P.2 mode) added on the interface of the ZnO/active layer (i.e., directly, in the active layer). In this case, the near-field images at selected wavelengths are given in Fig. 9 for Al and in Fig. S11 and S12 for Ag and Au, respectively. A qualitative comparison of Fig. 7, 8, and 9 show that the Al-P.2 MNS at the ZnO/active layer is associated with changes in the form of the near-field than Al-P.2 MNS at ITO/ZnO. In other words, the intensity of the backward near-field at the wavelengths of 400 nm and 500 nm has been reduced to a reasonable extent, and the intensity of the forward near-field at the wavelengths of 600 nm and 700 nm has been increased. These can be useful in designing solar cell enhancement due to the near-field effect. The same comparison between Fig. S8 and S11 also shows remarkable differences. The Ag-P.2 (at the interface of ITO/ZnO) parasitic absorption at wavelengths of 400 nm and 500 nm is no longer observed when they are inserted at the ZnO/Active layer. In the case of Au, the changes are somewhat reversed. On the other hand, in the Au-P.2 on ZnO/active layer, the parasitic absorption is intensified at 600 nm and 700 nm wavelengths than the ITO/ZnO case.

Shortly, in terms of the near-field effect, the Au case is numerically stronger, but it more appears in the form of parasitic absorption loss (Fig. S12 and S14). A slight parasitic absorption effect is seen to a small extent in the Ag sample, but its near-field amplifications are over a broader spectrum of wavelengths. In the Al case, it does not show parasitic absorption in the wavelength range.

The spectral reflection and the maximum field intensity of P.2 MNS (Al, Ag, and Au) on the interface of the ZnO/active layer are also shown in Fig. S13 and S14, respectively. Again, the reflectance difference is little than the standard sample.

4. Conclusion

In this study, the advanced FDTD model for MNS was presented. This model is based on some elliptical NPs whose average sizes and standard deviations are already determined. These particles are placed almost randomly together to form the MNS. The NP was divided into three groups O, P, and S, and these groups were divided into several modes based on the height of NP. Considering the average specifications and their standard deviation as well as the random rotation of the NPs relative to the vertical axis, different MNSs were prepared. This classification was made in such a way that the be close to experimental structures. It could represent different contact angles and the forms of MNS in some experimental methods. So, the results of this study could be useful in plasmonic designs. The results of the total reflectance of the modeled plasmonic samples and their comparison with the standard one as a criterion for investigating scattering (far-field effect) showed that none of them resulted in a significant reduction in reflectance across the whole spectrum. The maximum field intensity spectrum simulated on the selected cross-sections was chosen as a criterion for investigating the near-field effect. The results of this type were used to study the distributions of plasmonic peaks in the optical range, their scale, and to compare the effect of various modes and materials. The study has shown that for MNS at the interface of ITO/ZnO, the peak distribution of Al and Ag versus Au is broader over the spectrum. Instead, the numerical scale of Au is higher. Then, the field intensity image in the visible spectrum and with a step of 100 nm was used to more comparison the near-field effect. These images show the extent of the near-field effect in different directions around the NPs, the plasmonic coupling effects, and the field within the NPs themselves. These images showed that the amount of field distribution around the particle and the parasitic absorption is strongly dependent on the geometry of the MNS, wavelength, and its location. Al did not show much parasitic absorption in any mode and wavelength, unlike Au and Ag. Although the plasmonic effects of Au are greater, the parasitic absorption loss of Au must be carefully considered at each mode. Lastly, the same studies were repeated for P.2 mode when the MNS was placed at the interface of the ZnO/active layer. In fact, by adding MNS to the new location, changes are made in the near-field effects that they are not the continuation of the previous ones (when MNS was at the interface of ITO/ZnO). In general, the Au modeling of the MNS samples shows the effects of severe parasitic absorption loss. Generally, the Al and relatively Ag MNS at the interface of the ZnO/active layer can improve OSC performance due to optical reasons, especially by the near-field effect. Unlike Au and relatively Ag, the Al sample did not show the parasitic absorption loss for MNSs prepared by experimental methods.

Declarations

Acknowledgment

Thanks to Shahrekord University's rapid computing center for providing the simulation's hardware.

FUNDING

Not applicable

CONFLICTS OF INTEREST

The author declares no conflicts of interest.

AVAILABILITY OF DATA AND MATERIAL

Due to the increased size of the file after each simulation (usually about 50 GB or more), their storage is faced with hardware limitations.

CODE AVAILABILITY The Lumerical simulator is used for FDTD simulation.

AUTHORS' CONTRIBUTIONS Not applicable

ETHICAL APPROVAL Not applicable

CONSENT TO PARTICIPATE Not applicable

CONSENT FOR PUBLICATION Not applicable

References

1. Newton, D.E.: World Energy Crisis: A Reference Handbook. ABC-CLIO (2013)
2. Scales, A.J.: Civilization's Crisis: A Set Of Linked Challenges. World Scientific Publishing Company (2017)
3. Reinders, A., Verlinden, P., van Sark, W., Freundlich, A.: Photovoltaic Solar Energy: From Fundamentals to Applications, Wiley, 2017
4. Voronov, M.: Organic Solar Cells: Advances in Research and Applications. Nova Science Publishers, Incorporated (2017)
5. Berny, S., Blouin, N., Distler, A., Egelhaaf, H.-J., Krompiec, M., Lohr, A., Lozman, O.R., Morse, G.E., Nanson, L., Pron, A., Sauermann, T., Seidler, N., Tierney, S., Tiwana, P., Wagner, M., Wilson, H., Solar Trees: First Large-Scale Demonstration of Fully Solution Coated, Semitransparent, Flexible Organic Photovoltaic Modules, *Advanced Science*, 3: (2016) 1500342
6. Enrichi, F., Righini, G.C.: Solar Cells and Light Management: Materials, Strategies and Sustainability. Elsevier (2019)

7. Stuart, H.R., Hall, D.G.: Island size effects in nanoparticle-enhanced photodetectors. *Appl. Phys. Lett.* **73**, 3815–3817 (1998)
8. Zhou, N., López-Puente, V., Wang, Q., Polavarapu, L., Pastoriza-Santos, I., Xu, Q.-H.: Plasmon-enhanced light harvesting: applications in enhanced photocatalysis, photodynamic therapy and photovoltaics. *RSC Advances* **5**, 29076–29097 (2015)
9. Jang, Y.H., Jang, Y.J., Kim, S., Quan, L.N., Chung, K., Kim, D.H.: Plasmonic Solar Cells: From Rational Design to Mechanism Overview. *Chem. Rev.* **116**, 14982–15034 (2016)
10. Lim, E.L., Yap, C.C., Mat Teridi, M.A., Teh, C.H., Mohd Yusoff, A.R.b.: M.H. Hj Jumali, A review of recent plasmonic nanoparticles incorporated P3HT: PCBM organic thin film solar cells. *Org. Electron.* **36**, 12–28 (2016)
11. Ueno, K., Oshikiri, T., Sun, Q., Shi, X., Misawa, H.: Solid-State Plasmonic Solar Cells, *Chemical Reviews* **118**, 2955–2993 (2018)
12. Wu, B., Mathews, N., Sum, T.C.: *Plasmonic Organic Solar Cells: Charge Generation and Recombination*. Springer Singapore (2016)
13. Fedlheim, D.L., Foss, C.A.: *Metal Nanoparticles: Synthesis, Characterization, and Applications*, Taylor & Francis, 2001
14. Akimov, Y.A., Koh, W.S.: Resonant and nonresonant plasmonic nanoparticle enhancement for thin-film silicon solar cells. *Nanotechnology* **21**, 235201 (2010)
15. Qi, F.L., Xu, Y., Liu, W., Meng, K., Cui, X., Feng, W., Zhang, Huang, Y.: Aluminum plasmonic nanoparticles enhanced dye sensitized solar cells. *Opt. Express* **22**, A301–A310 (2014)
16. Dusastre, V.: *Materials for Sustainable Energy: A Collection of Peer-reviewed Research and Review Articles*. from Nature Publishing Group, World Scientific (2011)
17. Knight, M.W., King, N.S., Liu, L., Everitt, H.O., Nordlander, P., Halas, N.J., Aluminum for Plasmonics, *ACS Nano*, 8: (2014) 834–840
18. Gérard, D., Gray, S.K.: *Special Issue on Aluminium Plasmonics*. IOP Publishing (2015)
19. Haber, J.A., Buhro, W.E.: Kinetic Instability of Nanocrystalline Aluminum Prepared by Chemical Synthesis; Facile Room-Temperature Grain Growth. *J. Am. Chem. Soc.* **120**, 10847–10855 (1998)
20. Martin, J., Plain, J.: Fabrication of aluminium nanostructures for plasmonics. *J. Phys. D: Appl. Phys.* **48**, 184002 (2014)
21. Lachebi, I., Fedala, A., Djenizian, T., Hadjersi, T., Kechouane, M.: Morphological and optical properties of aluminum nanoparticles deposited by thermal evaporation on heated substrates. *Surface and Coatings Technology* **343**, 160–165 (2018)
22. Fredriksson, H., Alaverdyan, Y., Dmitriev, A., Langhammer, C., Sutherland, D.S., Zäch, M., Kasemo, B.: Hole–Mask Colloidal Lithography, *Advanced Materials* **19**, 4297–4302 (2007)
23. Inan, U.S., Marshall, R.A.: *Numerical Electromagnetics: The FDTD Method*, Cambridge University Press, 2011

24. Yu, W., *Advanced, F.D.T.D., Methods: Parallelization, Acceleration, and Engineering Applications*, Artech House, 2011
25. Das, N., *Nanostructured Solar Cells*, IntechOpen, 2017
26. Feng, L., Niu, M., Wen, Z., Hao, X.: Recent Advances of Plasmonic Organic Solar Cells, p. 10. *Photophysical Investigations, Polymers* (2018)
27. Gaspar, D., Pimentel, A.C., Mateus, T., Leitão, J.P., Soares, J., Falcão, B.P., Araújo, A., Vicente, A., Filonovich, S.A., Águas, H., Martins, R., Ferreira, I.: Influence of the layer thickness in plasmonic gold nanoparticles produced by thermal evaporation. *Sci. Rep.* **3**, 1469 (2013)
28. Parashar, P.K., Sharma, R.P., Komarala, V.K.: Plasmonic silicon solar cell comprised of aluminum nanoparticles: Effect of nanoparticles' self-limiting native oxide shell on optical and electrical properties. *J. Appl. Phys.* **120**, 143104 (2016)
29. Rockett, A.: *THIN FILM GROWTH PROCESSES*, in: *The Materials Science of Semiconductors*. Springer US (2007)
30. Heilmann, A.: *Polymer Films with Embedded Metal Nanoparticles*. Springer, Berlin Heidelberg (2013)
31. Quan, J., Zhang, J., Qi, X., Li, J., Wang, N., Zhu, Y.: A study on the correlation between the dewetting temperature of Ag film and SERS intensity. *Sci. Rep.* **7**, 14771 (2017)
32. Gonçalves, M.R., Melikyan, A., Minassian, H., Makaryan, T., Marti, O.: Strong dipole-quadrupole coupling and Fano resonance in H-like metallic nanostructures. *Opt. Express* **22**, 24516–24529 (2014)
33. Shopa, M., Kolwas, K., Derkachova, A., Derkachov, G.: Dipole and quadrupole surface plasmon resonance contributions in formation of near-field images of a gold nanosphere. *Opto-Electron. Rev.* **18**, 421–428 (2010)

Figures

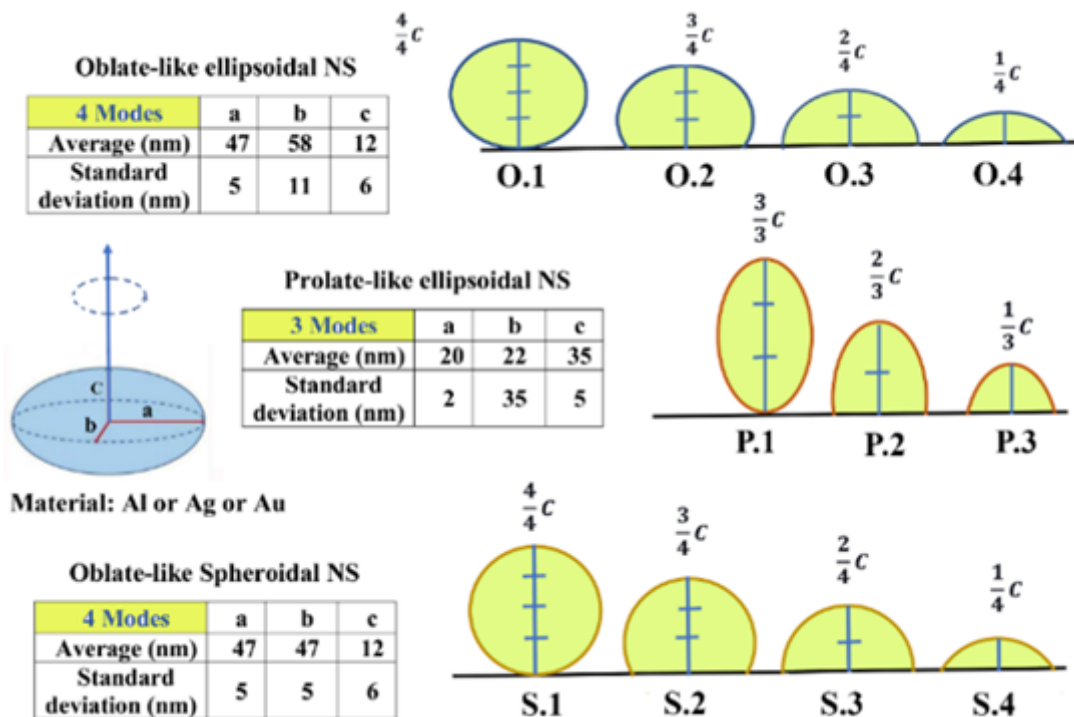


Figure 1

Show the three groups O, P, and S. They refer to “oblate”, “prolate” and “spherical” particles, respectively. The geometric characteristics of each group are mentioned in the tables. Each group has some modes that differ only in the vertical particle size (here ‘c’ axes). Simulations are done separately for each mode and material (Al, Ag, and Au). the pre-determined average particle size and standard deviation are listed for each group.

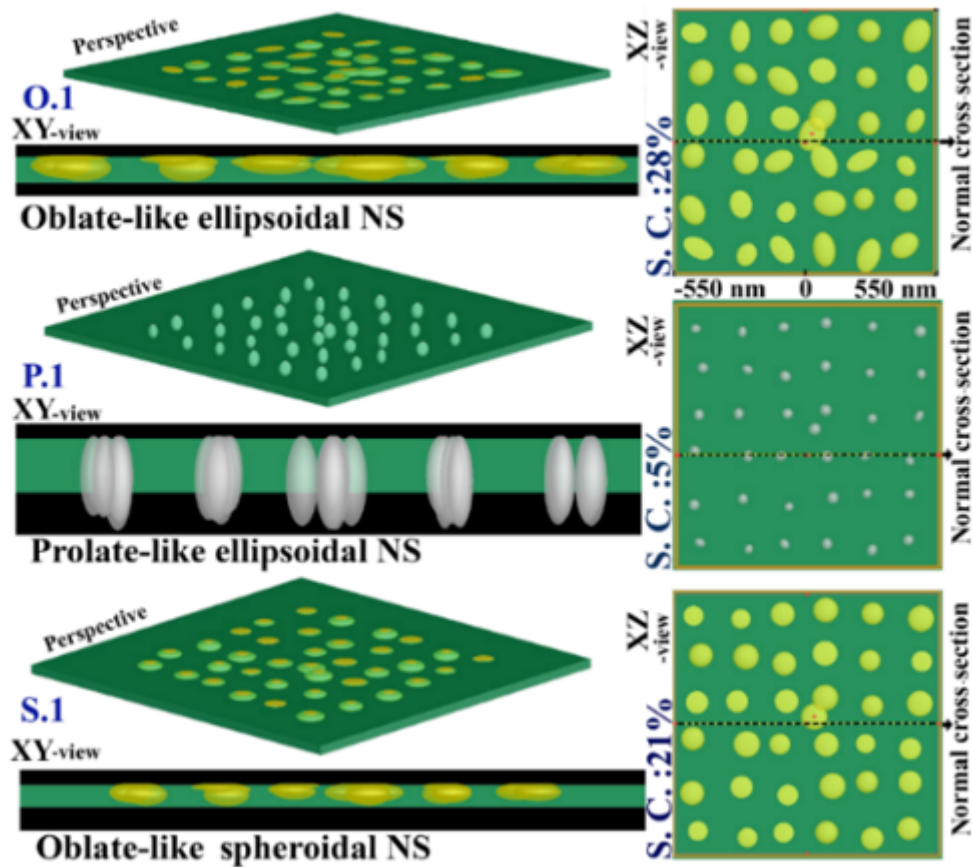


Figure 2

Perspectives and XY-XZ view of mode1 for the three groups (O, P, and S). The XZ-view shows the surface on which the particles have the largest lateral diameter. In this case, the percentage of surface coverage (S. C.) was also reported. The selected (typical) normal cross-sections (includes axes Y and Z) were shown as a dotted line. In O.1 and S.1, they contain, only a part of one particle of MNS. But, P.1 includes several particles.

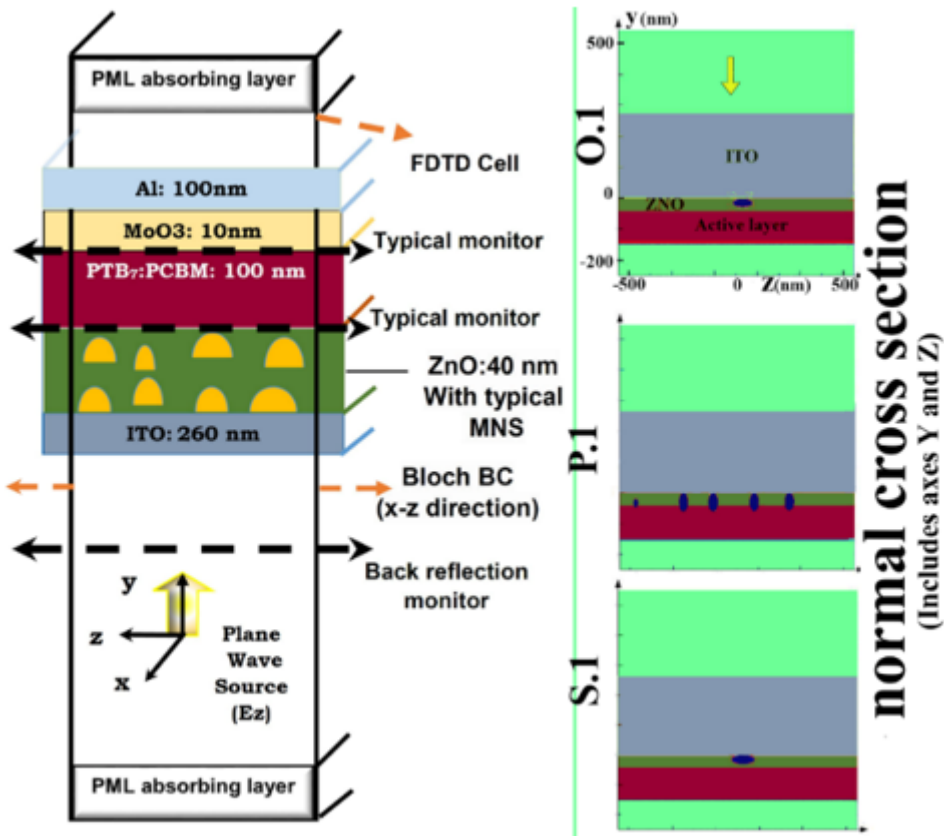


Figure 3

View of the 3D FDTD region. In the inset, three normal cross-sections are shown, that they are also pointed as the dotted lines in Fig. 2. In the simulation, near-field results are calculated on these slices.

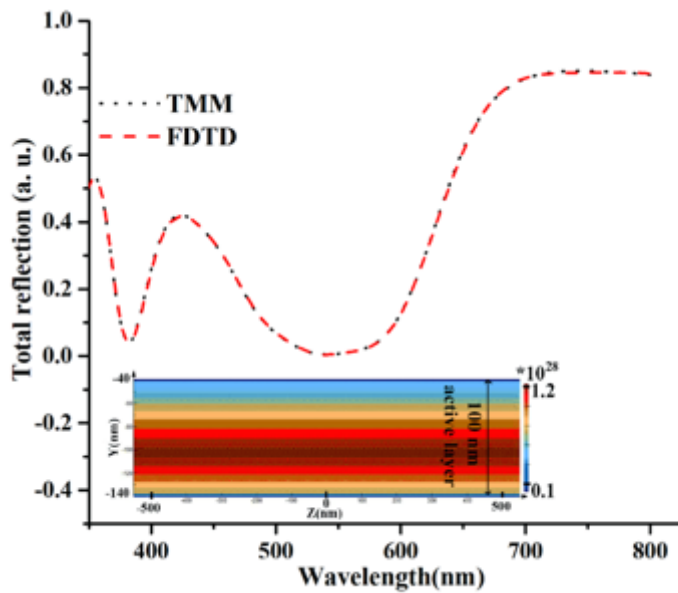


Figure 4

The total spectral reflection (backward scattering) of the standard cell surface was calculated by TMM and FDTD methods. The inset shows the generation rate profile of the standard cell.

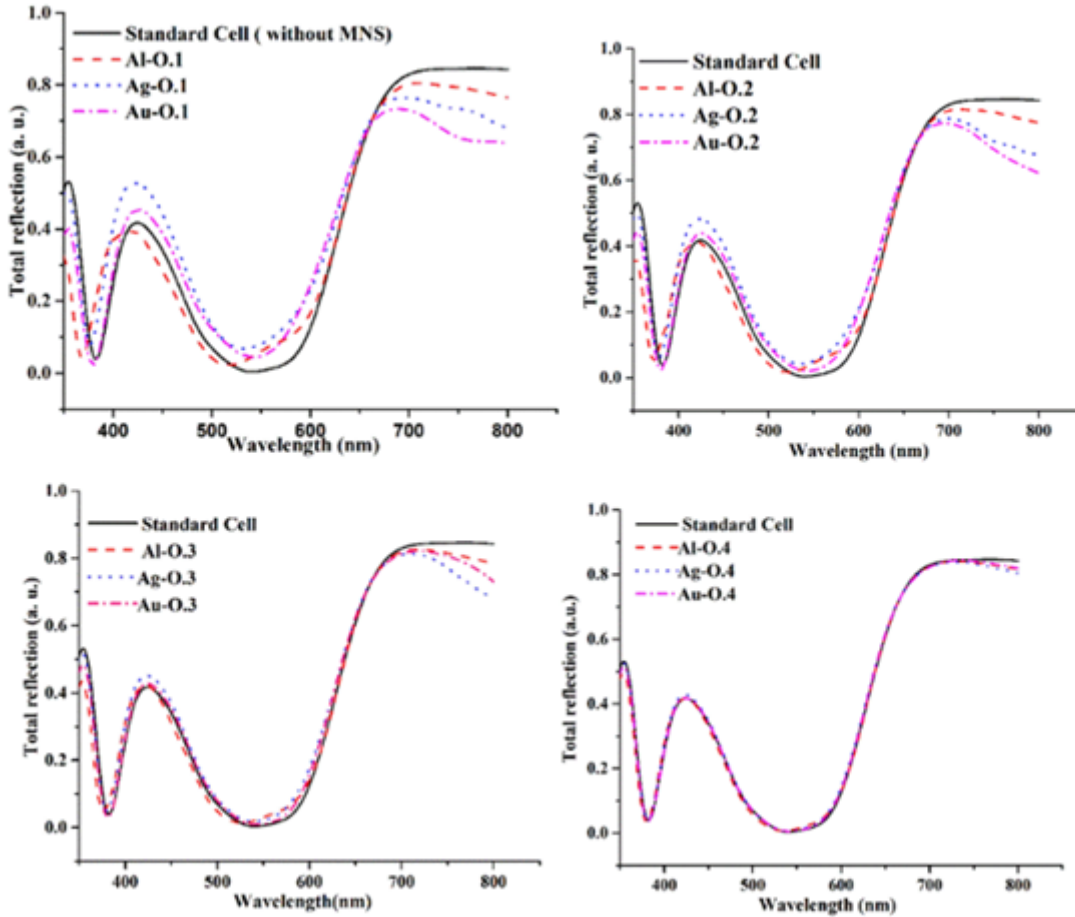


Figure 5

The total spectral reflection (backward scattering or far-field result) of the plasmonic OSC (MNS at the interface of ITO/ZnO). The MNS is modeled with a different mode of O-group (0.1 until 0.4). The material of MNS is Al, Ag, and Au.

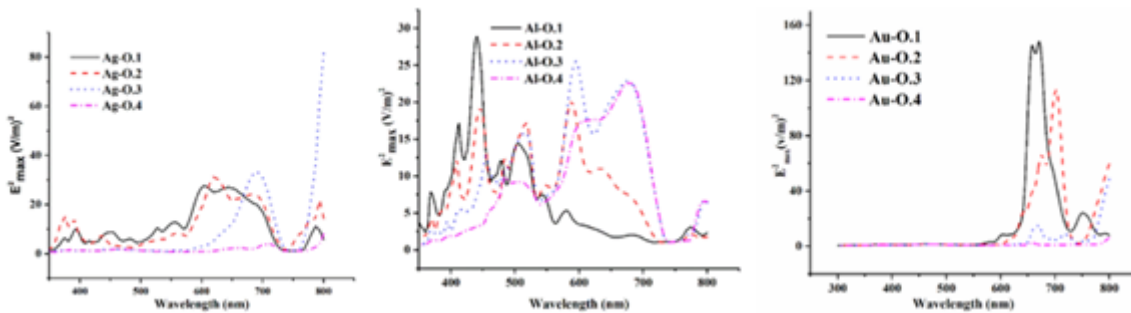


Figure 6

The maximum field intensity simulated at each wavelength on the selected cross-section for the four modes of O-group and different materials Al, Ag, and Au (MNS at the interface of ITO/ZnO).

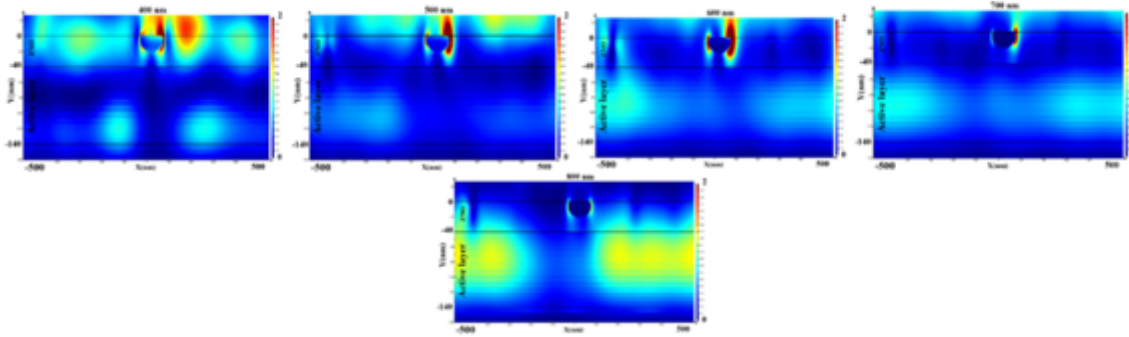


Figure 7

Images of field intensity at different wavelengths (400 nm, 500 nm, 600 nm, 700 nm, and 800 nm) on the selected cross-section of the Al-O.2 mode (MNS at the interface of ITO/ZnO).

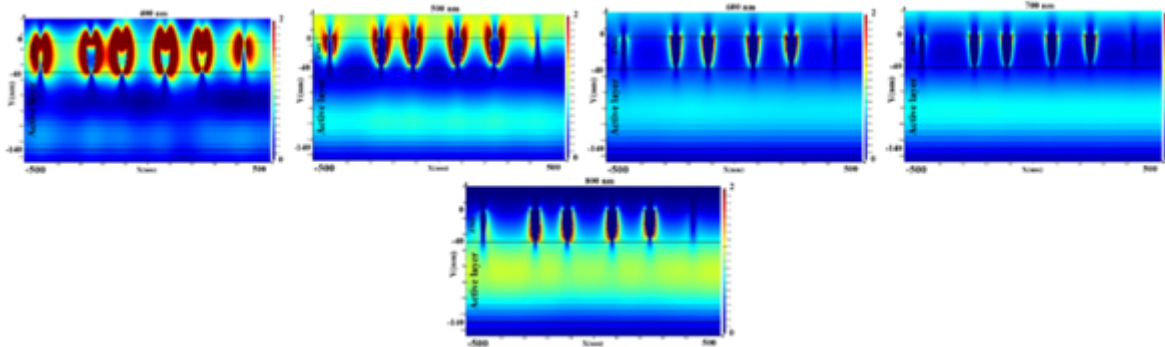


Figure 8

Images of field intensity at different wavelengths (400 nm, 500 nm, 600 nm, 700 nm, and 800 nm) on the selected cross-section of the Al-P.2 mode (MNS at the interface of ITO/ZnO).

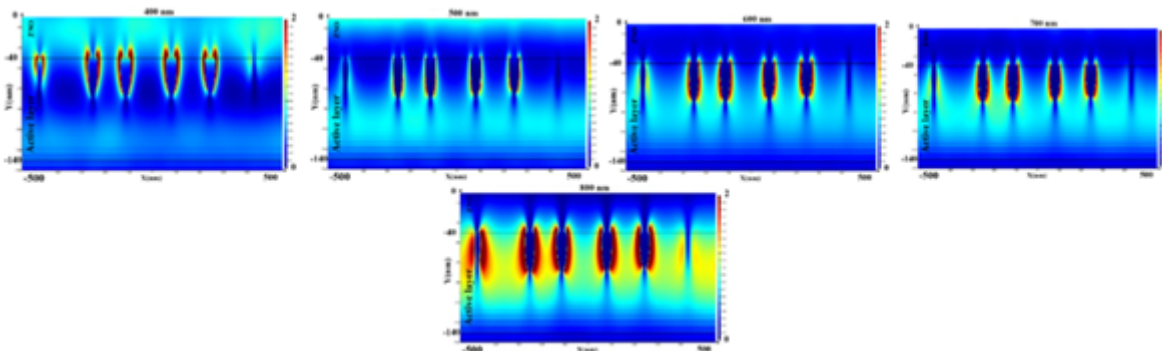


Figure 9

Images of field intensity at different wavelengths (400 nm, 500 nm, 600 nm, 700 nm, and 800 nm) on the selected cross-section that the Al-P.2 MNS was added to the interface of the ZnO/active layer.

Supplementary Files

This is a list of supplementary files associated with this preprint. Click to download.

- [SupplementaryMaterial.docx](#)